HHS Public Access

Author manuscript

Nature. Author manuscript; available in PMC 2020 December 12.

Published in final edited form as:

Nature. 2020 May ; 581(7807): 209–214. doi:10.1038/s41586-020-2256-2.

Composition dependent thermodynamics of intracellular phase separation

Joshua A. Riback[1,#], **Lian Zhu**[1,#], **Mylene C. Ferrolino**[2], **Michele Tolbert**[2], **Diana M. Mitrea**[2,‡], **David W. Sanders**[1], **Ming-Tzo Wei**[1], **Richard W. Kriwacki**[2,*], **Clifford P. Brangwynne**[1,3,4,*]

[1]Department of Chemical and Biological Engineering, Princeton University, Princeton, NJ 08544, USA

[2]Department of Structural Biology, St. Jude Children's Research Hospital, Memphis, TN 38103, USA

[3]Lewis Sigler Institute for Integrative Genomics, Princeton University, Princeton, NJ 08544, USA

[4]Howard Hughes Medical Institute

Abstract

Intracellular bodies such as nucleoli, Cajal bodies, and various signaling assemblies, represent membraneless organelles, or condensates, that form via liquid-liquid phase separation (LLPS)[1,2]. Biomolecular interactions, particularly homotypic interactions mediated by self-associating intrinsically disordered protein regions (IDRs), are thought to underlie the thermodynamic driving forces for LLPS, forming condensates that can facilitate the assembly and processing of biochemically active complexes, such as ribosomal subunits within the nucleolus. Simplified model systems[3–6] have led to the concept that a single fixed saturation concentration (C_{sat}) is a defining feature of endogenous LLPS[7–9], and has been suggested as a mechanism for intracellular concentration buffering[2,7,8,10]. However, the assumption of a fixed C_{sat} remains largely untested within living cells, where the richly multicomponent nature of condensates could complicate this simple picture. Here we show that heterotypic multicomponent interactions dominate endogenous LLPS, and give rise to nucleoli and other condensates that do not exhibit a fixed C_{sat}. As the concentration of individual components is varied, their partition coefficients change, in a manner that can be used to determine thermodynamic free energies underlying LLPS. We find that

[*]Corresponding Authors, cbrangwy@princeton.edu; richard.kriwacki@stjude.org.
[‡]Current Address: Dewpoint Therapeutics, Boston, MA 02210, USA
[#]Equal contribution

Author Contributions

J.A.R, L.Z., D.M.M., R.W.K. and C.P.B. designed research; *In vivo* studies were performed and analyzed by J.A.R., L.Z., D.W.S., and M.W.; *In vitro* studies were performed and analyzed by M.C.F., M.T., and D.M.M.; J.A.R, L.Z., and C.P.B. wrote, and all authors reviewed and edited the paper.

Data availability:

Source data for Figures 1–4 and Extended Data Figures 1, 2, 3–8 are available with the paper. All other data are available from the corresponding authors upon request.

Declaration of Interests

R.W.K. is a consultant for and D.M.M. is recently employed by Dewpoint Therapeutics, LLC. The remaining authors have no financial or non-financial conflicts of interest.

Additional information

Supplementary information is available for this paper at https://doi.org/10.1038/s41586-020-2256-2

heterotypic interactions among protein and RNA components stabilize a variety of archetypal intracellular condensates, including the nucleolus, Cajal bodies, stress granules, and P bodies. These findings imply that the composition of condensates is finely tuned by the thermodynamics of the underlying biomolecular interaction network. In the context of RNA processing condensates such as the nucleolus, this manifests in selective exclusion of fully-assembled RNP complexes, providing a thermodynamic basis for vectorial ribosomal RNA (rRNA) flux out of the nucleolus. This methodology is conceptually straightforward and readily implemented, and can be broadly utilized to extract thermodynamic parameters from microscopy images. These approaches pave the way for a deep understanding of the thermodynamics of multi-component intracellular phase behavior and its interplay with nonequilibrium activity characteristic of endogenous condensates.

To determine the thermodynamics of LLPS for intracellular condensates we first focused on the liquid granular component (GC) of nucleoli within HeLa cells, in particular on the protein Nucleophosmin (NPM1), which is known to be a key driver of nucleolar phase separation[11,12]. Under typical endogenous expression levels, we estimate NPM1 concentration in the nucleoplasm to be roughly C^{dil}~4 μM; from simple binary phase separation models (*i.e.* Regular solution theory, Supplemental Note 1)[13], this apparent saturation concentration, C_{sat}, is expected to be fixed even under varied protein expression levels (Fig. 1C). Consistent with previous studies[11], overexpression of NPM1 resulted in larger nucleoli, underscoring the importance of NPM1 in nucleolar assembly (Fig. 1A). However, with these increased levels of NPM1, the nucleoplasmic concentration did not remain fixed at a single C_{sat}, but instead increased by roughly 10-fold (Fig. 1B **and** Supplemental Note 2). Interestingly, the NPM1 concentration within the dense phase nucleolus, C^{den}, also increases, but the ratio of the dense to dilute concentrations, known as the partition coefficient $K = \frac{C^{den}}{C^{dil}}$, decreased significantly (Extended Data Fig. 1).

To elucidate the underlying biophysics of this observed non-fixed C_{sat} within living cells, we examined phase separation of model biomimetic condensates not natively present within the cell. We took advantage of the optoDroplet system[4], developed for controlling intracellular phase separation, by fusing the blue-light-dependent higher-order oligomerizing protein Cry2 to the IDR of DDX4, which drives phase separation of exogenous condensates through predominately homotypic interactions[3,4,10]. Consistent with our prior work[14], at total cellular concentrations above ~1.7 μM, light activates droplet formation, and nucleoplasmic and cytoplasmic C^{dil} remains at a fixed value, suggesting a fixed C_{sat}~1.7 μM (Fig. 1D-E). We next asked whether a fixed C_{sat} would be observed with light induction of stress granules, multi-component, stress-inducible condensates which assemble through heterotypic protein-mRNA interactions[15]. We replaced the oligomerization domain of G3BP1, a critical stress granule protein, with Cry2, and expressed this construct in G3BP1/2 knockout cells under arsenite stress. At total cytoplasmic concentrations above ~0.7 μM, light triggers droplet formation; however, unlike the synthetic DDX4 case, the C^{dil} was not fixed, but instead increased with increasing total concentrations (Fig. 1D,F), similar to the behavior of NPM1 (Fig. 1A,B). These results are not restricted to light-induced oligomerization of G3BP1 using the optogenetic system, as increasing expression of G3BP1 in a G3BP1/2 KO cell line exhibits a similar increase in the C^{dil} (Extended Data Fig. 2A).

These data suggest that multicomponent condensates are not governed by a fixed C_{sat}, as expected for a single biomolecule component (*i.e.* binary solution when including the solvent, Supplemental Note 1) phase boundary at fixed temperature. Instead, endogenous condensates may be governed by the more richly textured thermodynamics dictating higher dimensional phase diagrams (Fig. 1C), consistent with theoretical and experimental findings on model multicomponent systems[13,16–22]. To probe this concentration-dependent thermodynamics, we quantify the effect of increasing concentration of a biomolecule *in vivo* or *in vitro*, which shifts stoichiometry to bias towards more homotypic interactions (Fig. 2A, Extended Data Fig. 3, Supplemental Note 3). This changes the partition coefficient, allowing us to quantify changes in the generalized standard free energy of transfer for any component from the dilute to the dense phase, here denoted as ΔG^{tr} (Fig. 2B); thermodynamic considerations yield the relationship $\Delta G^{tr} = -RT \ln K$ (Supplemental Note 4). For components which contribute to phase separation (*e.g.* act to scaffold the condensate meshwork), their transfer free energy reports on the stability of interactions driving phase separation.

Applying this framework to our NPM1 results (Fig. 1A-B), as the NPM1 concentration is increased, the partition coefficient of NPM1 into the nucleolus decreases (Extended Data Fig. 1B), and thus the transfer free energy ΔG^{tr} for NPM1 between the condensed and dilute phases becomes less negative, and thus destabilizing; this destabilizing effect at higher NPM1 concentrations implies that heterotypic, rather than homotypic (*i.e.* NPM1-NPM1), interactions dominate endogenous nucleolar assembly (Fig. 2C). To further test this conclusion, we focused on *in vitro* reconstitution of the nucleolar GC. In addition to NPM1, key GC components include ribosomal RNA (rRNA), and multivalent poly-arginine motif-containing proteins (Arg-proteins) such as SURF6, and ribosomal proteins (r-proteins). Utilizing a well-established system for GC phase separation *in vitro*[11,12,20,23], we formed either NPM1-only droplets with 5% PEG as a crowder (Fig. 2D, **bottom image**) or multicomponent droplets containing NPM1, the N-terminus of SURF6 (SURF6N), and rRNA (Fig. 2D, **upper image**). As expected for single biomolecule component phase separation, as more NPM1 was added to the NPM1-only droplets, the transfer free energy remained roughly constant (Fig. 2D, **green data**). In contrast, for multicomponent droplets, the transfer free energy became significantly less negative (*i.e.* destabilizing) as more NPM1 was added, exactly as observed in living cells (Fig. 2D, **black data**).

Remarkably, similar behavior in cells was observed with a number of different intracellular condensates and their associated key scaffolding proteins: Coilin in Cajal bodies, G3BP1 in arsenite-triggered stress granules, and DCP1A in P-Bodies; in each of these cases, increasing protein concentrations yielded larger condensates, surrounded by a higher C^{dil}, and with correspondingly less negative transfer free energies (Fig. 2E-G, Extended Data Fig. 2); these data are consistent with previous studies highlighting the complex nature of biomolecule recruitment to *in vitro* and *in vivo* reconstituted condensates[12,24]. However, our findings contrast with the view that condensates are stabilized by predominantly homotypic interactions, for example those mediated by self-associating IDRs. Instead, this suggests heterotypic interactions play a central role in promoting the internal cohesivity stabilizing LLPS, not only for nucleoli but also for other intracellular condensates.

We next probed which heterotypic interactions drive phase separation of the nucleolus, by monitoring one component's transfer free energy while changing the concentration of another (Fig. 3A). In our multicomponent *in vitro* mimic, we find that increasing NPM1 or SURF6N makes the partitioning of SURF6N less energetically favorable (Extended Data Fig. 4), again consistent with heterotypic interactions driving SURF6 to nucleoli. In living cells, SURF6 also exhibits behavior similar to NPM1, with a destabilizing increase in the transfer free energy observed with increasing SURF6 concentration (Fig. 3C, black lines). Interestingly, this *in vivo* destabilization is dramatically amplified with increasing NPM1 concentrations (Fig. 3B-C). From these data, we determined the change in the transfer free energy of SURF6 as a function of NPM1 by referencing to the energy expected without NPM1 overexpression, *i.e.* $\Delta G^{tr}_{SURF6}([NPM1]_{dil})=\Delta G^{tr}_{SURF6}([NPM1]^{dil},[SURF6]^{dil})-\Delta G^{tr}_{SURF6}([NPM1]^{dil}=0,[SURF6]^{dil})$. Remarkably, plotting $\Delta\Delta G^{tr}_{SURF6}$ vs. NPM1 collapses the data onto a single master curve (Fig. 3D, Methods), highlighting a tight thermodynamic linkage between NPM1 and SURF6. This behavior contrasts with that of ribosomal proteins (r-proteins), which exhibit strong and specific rRNA binding, and exhibit a transfer free energy which is statistically insensitive to NPM1 concentrations (Extended Data Fig. 5).

Both SURF6 and NPM1 have been proposed to interact with rRNA through weak promiscuous binding[12] and we thus hypothesized that SURF6-NPM1 linkage occurs as a consequence of heterotypic interactions with rRNA, which are diluted upon NPM1 overexpression. To test whether heterotypic interactions with rRNA underlie the thermodynamics of nucleolar assembly, we performed our analysis in cells following actinomycin D (ActD) treatment, which is known to halt transcription of nascent rRNA without affecting processing and assembly of pre-existing rRNA[25,26] (Fig. 3E). As previously reported, the addition of ActD results in the progressive reduction of nucleolus size over the course of 4 hours (Fig. 3F, Extended Data Fig. 6)[27]. Over time, the $\Delta\Delta G^{tr}$ of NPM1 and SURF6 increases, indicating weakened interactions relative to cells without ActD, consistent with NPM1 and SURF6 driving heterotypic phase separation through multivalent interactions with nascent, unfolded (or misfolded) rRNA transcripts, which become increasingly scarce under ActD treatment. Conversely, we find that the two r-proteins RPL23A and RPL5 display the opposite behavior, with their transfer free energies decreasing with the progression of ActD treatment (Fig. 3G,H), reflecting strengthened interactions that are consistent with specific binding to more fully processed rRNA.

These findings shed light on how heterotypic interactions driving phase separation facilitate sequential rRNA processing in ribosome biogenesis. Specifically, relatively nascent rRNA transcripts are available for more interactions with NPM1, SURF6, and other scaffolding components of the GC-matrix, compared to fully assembled ribosome subunits, providing a mechanism to facilitate the vectorial flux of processed subunits out of the nucleolus (Fig. 4F). Indeed, binding of nascent transcripts by r-proteins eliminates multivalent binding sites for heterotypic scaffolding proteins, which could serve to effectively expel fully assembled pre-ribosomal particles. We tested this concept using the biomimetic Corelet system, which consists of a 24-mer ferritin core, where each ferritin subunit is fused to an optogenetic heterodimerization domain, which can be used to tune the effective valency of the particle with light[6] (Fig. 4A). We fused the optogenetic protein to an N-terminal truncated NPM1 (NPM1-C; residues 120–294), thus allowing light-dependent multivalent interactions with

the nucleolus. On its own, this construct partitions only weakly into nucleoli, with a ΔG^{tr} of approximately −0.4 kcal/mol (Extended Data Fig. 7). In the absence of bound NPM1-C, the ferritin core is strongly excluded from nucleoli, with a ΔG^{tr} of approximately +1.4 kcal/mol (Extended Data Fig. 7), consistent with large non-interacting assemblies being excluded from the nucleolus and other condensates[28–30]. However, upon increasing the valence of the core with light activation, its partitioning into the nucleolus increases, implying a more favorable (*i.e.* negative) transfer free energy. This effect depends strongly on the valence of the Core: for valence <10 Corelets are excluded ($\Delta G^{tr}>0$), while for valence >10 Corelets are enriched ($\Delta G^{tr}<0$) within the nucleolus (Fig. 4B-C **and** Extended Data Fig. 7). This physical picture is supported by *in vitro* experiments with NPM1 droplets and *E. coli* ribosomal components, which reveal that ΔG^{tr} is more strongly negative for 16S rRNA, compared to the 30S ribosomal subunit (comprised of 16S plus associated r-proteins Extended Data Fig. 8A-C) (Fig. 4E). Consistent with these measurements, *in vitro* phase separation of NPM1 is significantly weaker in the presence of the 30S subunit compared with 16S rRNA (Fig. 4D), underscoring how non-ribosomal protein bound (*i.e.* smaller) and highly solvent-exposed rRNAs are associated with favorable heterotypic interactions that promote partitioning and phase separation with nucleolar scaffold proteins (Fig. 4D-E). Similarly, *in vitro* phase separation was significantly weaker in the presence of the full 70S ribosome compared with either 23S rRNA or total (*i.e.* 23S, 16S, and 5S) rRNA (Extended Data Fig. 8D). All together, these data suggest a mechanism that links the ability of nascent rRNA to promote phase separation and concentrate within nucleoli, while explaining how interactions with fully assembled ribosomal subunits are disfavored, leading to their thermodynamically-driven exit from nucleoli.

Our findings lay the groundwork for a quantitative understanding of the interplay between composition-dependent thermodynamics of condensate assembly and the free energy landscape of biomolecular complex assembly. In particular, we show that heterotypic biomolecular interactions give rise to high-dimensional phase behavior that yields C_{sat} values that vary with component concentrations, providing a mechanism for tuning condensate composition. This enables “on demand” condensate assembly, such that phase separation only occurs in the presence of substrate, while simultaneously enabling a non-equilibrium steady-state flux of products (substrates), which are driven out of (or in to), the condensate during processing. This is likely relevant not only to the nucleolus, but also to many other phase-separated condensates that facilitate the formation of diverse biomolecular complexes, such as the spliceosome. Future work will exploit these intracellular thermodynamic self-assembly principles towards novel organelle engineering applications.

Extended Data

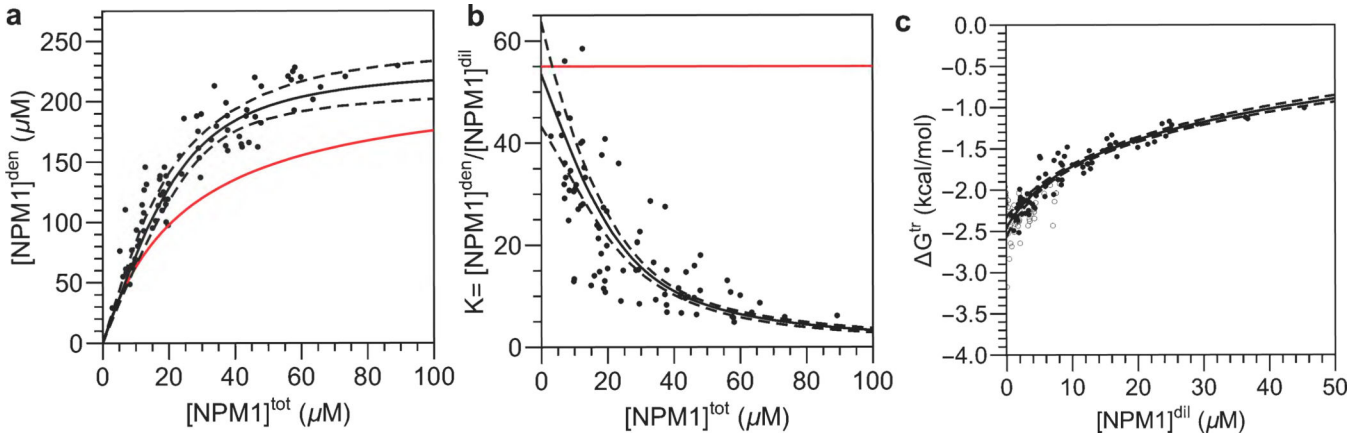

Figure 1. NPM1 lacks a fixed C^{dil} and C^{den} suggesting nucleoli undergo multicomponent mediated phase separation.

(A-B) Dependence of NPM1 total overexpression in the nucleus vs. (A) its measured concentration in the relevant dense phase (here 'den' referring to the GC of nucleoli) or (B) its apparent partition coefficient (*i.e.* the ratio of its concentration in the dense and dilute phases). (C) Dependence of the transfer free energy with increasing NPM1 in the dilute phase for mCherry (filled circles) vs. mGFP (open circles) tagged protein highlighting similar trends for the different florescent tagged proteins. Dashed lines represent mean confidence intervals to fits described in the methods. Red lines represent expected trends for single biomolecule phase separation.

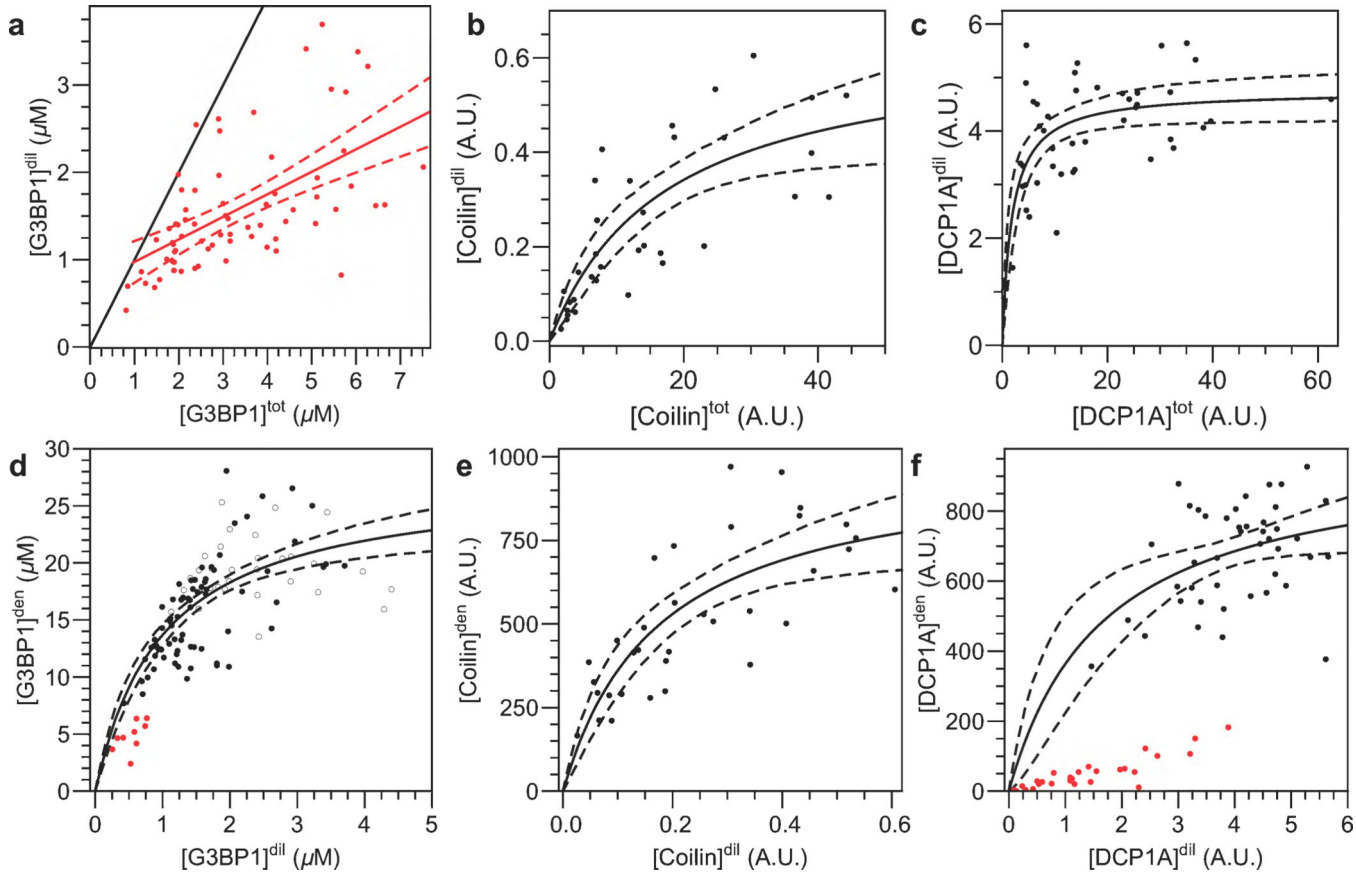

Figure 2. G3BP1, Coilin, and DCP1A lack fixed C^{dil} and C^{den} in cells.

Relationship between the approximated total concentration and the dilute concentration for cells expressing variable amounts of fluorescently tagged (A) G3BP1, (B) Coilin, and (C) DCP1A. Relationship between the dilute and dense concentrations for cells expressing variable amounts of fluorescently tagged (D) G3BP1, (E) Coilin, and (F) DCP1A. Dashed lines represent mean confidence intervals to fits described in the methods. Statistical significance ($p<0.01$) for these increasing monotonic relationships between the axes are reported in the methods. Red points in (D) and (F) represent diffraction limited foci.

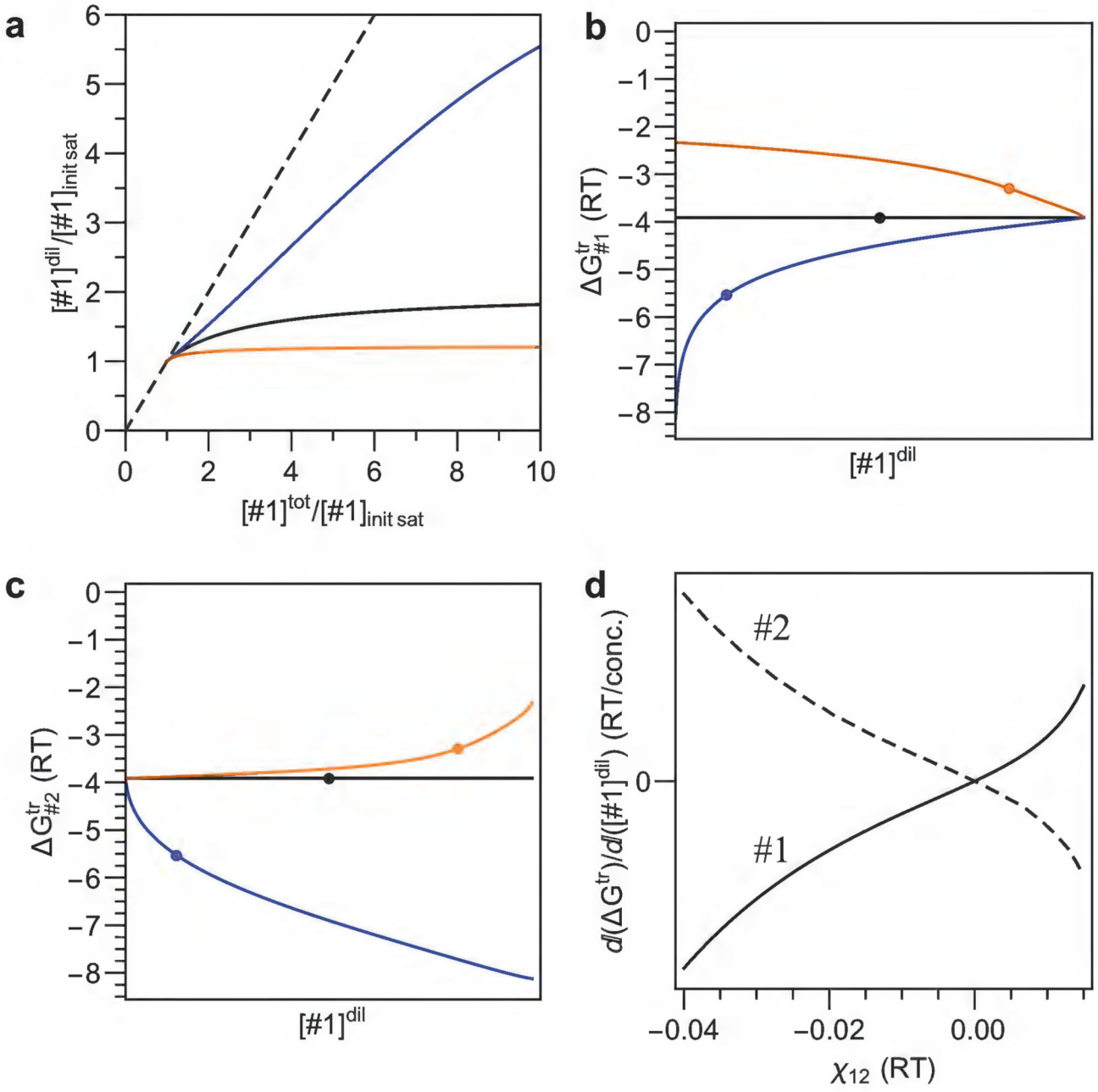

Figure 3. *In silico* validation of the composition-dependence of phase separation using Flory Huggins theory.

Phase separation of two (non-solvent) components, denoted #1 and #2, with their heterotypic interactions being equal, stronger, and weaker, then their homotypic interactions shown as black, blue, and orange, respectively for A-C. Note the dilute phase in the bottom left corner of the plot. (A) The initial dependence of the $[\#1]^{dil}$ on $[\#1]^{tot}$ at fixed $[\#2]^{tot}$ such that phase separation will occur at the 'goldilocks point' being when $[\#1]^{tot}=[\#2]^{tot}$. Note the axes are normalized by the initial saturation (init sat) concentration, *i.e.* lowest $[\#1]^{tot}$ where phase separation emerges. The dashed line is the 1:1 line where expected without phase separation. (B,C) Dependence on $\Delta G^{tr}_{\#1}$ (D) or $\Delta G^{tr}_{\#2}$ (E) as a function of $[\#1]^{dil}$. Circles indicate the

location of the 'goldilocks point'. (D) Dependence of the change in ΔG^{tr} with respect to $[\#1]^{dil}$ as a function of the heterotypic interaction strength χ_{12} (where more negative implies stronger heterotypic interactions) at the 'goldilocks point' for the transfer free energy of #1 and #2 as indicated.

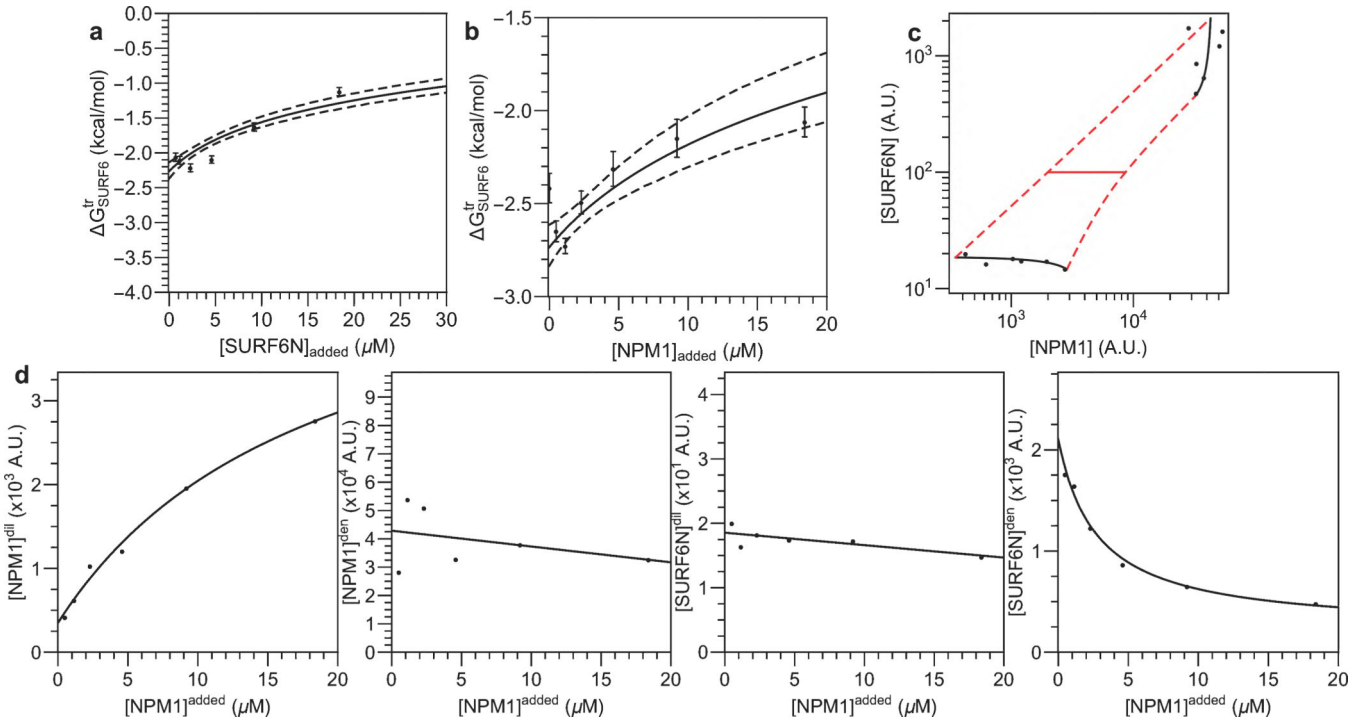

Figure 4. *In vitro* destabilization of SURF6N partitioning by increasing its own or NPM1's concentration.

Changes in the transfer free energy of SURF6N into multicomponent droplets as additional SURF6N (A) or NPM1 (B) is added on top of NPM1:SURF6N:rRNA ternary droplets as described in the methods. The number of droplets (in order of concentration) are N=122, 115, 105, 98, 98, 91, 74, and 99. Mean and standard deviation of error bars are shown. (C) Phase diagram *in vitro* in the presence of 25 ng/μL wheatgerm rRNA, 5 μM SURF6N, and various concentrations of NPM1. Units shown are absorbance units corrected for background, quantum yield differences between the two phases, and the (non-linear) fraction labeled of NPM1. (D) Dependences of the phase diagram as additional NPM1 is added. As in C, NPM1 concentrations in the dense or dilute phases are indicative of total NPM1. Hyperbolic fits shown highlight that the largest changes with NPM1 addition are from an increase in NPM1's dilute phase concentration and a decrease in SURF6N's dense phase concentration. To assess significance, yaxes in D are shown from zero arbitrary units (A.U.) to 2.5 times the mean of all points shown.

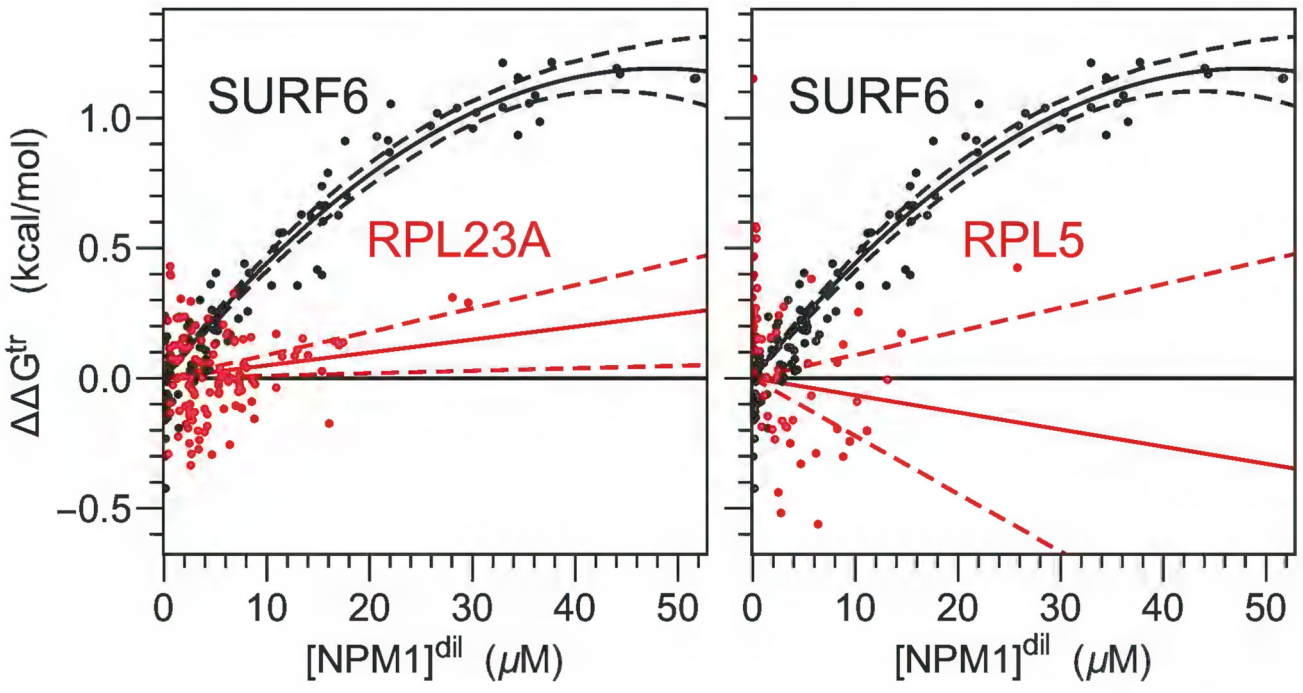

Figure 5. R proteins and NPM1 $\Delta\Delta G^{tr}$.

Change in the transfer free energy of r-proteins RPL23A and RPL5 compared to that for SURF6 as NPM1 concentration is increased.

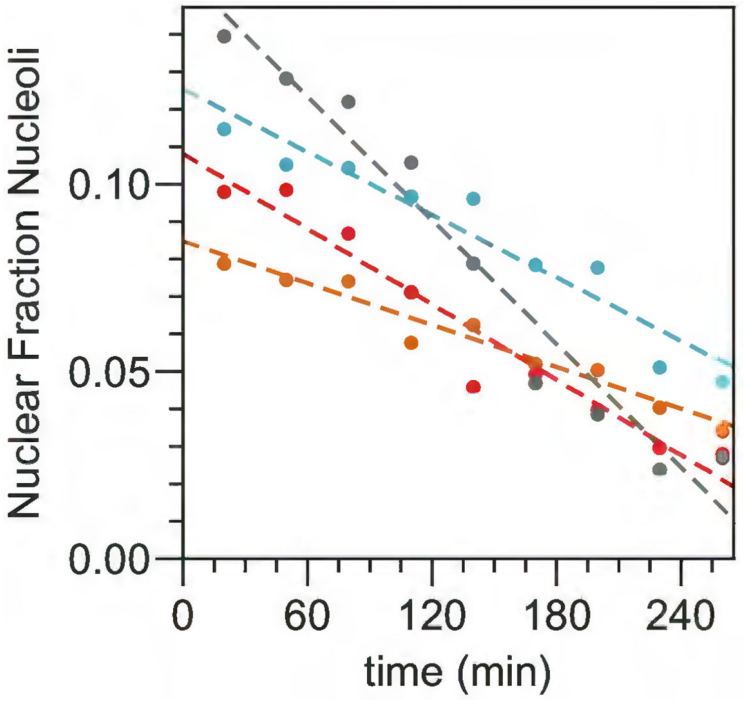

Figure 6. ActD decreases nucleolus size.

Nucleolar fraction of image area as a function of time after addition of ActD in individual cells expressing NPM1-mCherry. Colors indicate same cells as in Fig. 3G, right.

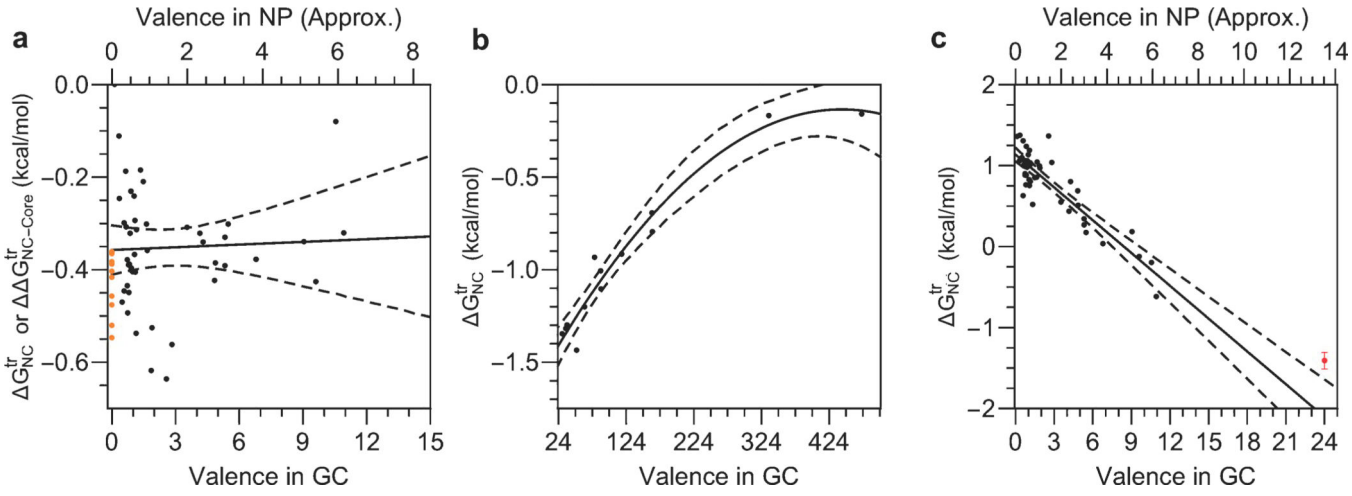

Figure 7. Characterization of Corelet non-ideality and extrapolation from high valence.

(A) Dependence on the transfer free energy for the N-terminal half of NPM1 (NC)-sspB in cells without the core expressed (orange being a ΔG^{tr}) or with the indicated valences following core activation (black being a $\Delta\Delta G^{tr}_{NC\text{-}Core}$). The $\Delta\Delta G^{tr}_{NC\text{-}Core}$ in this case is the energetic difference between the NC and core channels which is approximately the energetic difference for transferring an additional NC to the core at that valence. (B) At valences higher then 24, the transfer free energy is approximated as quadratic and extrapolated back to a valence of 24 to obtain the transfer free energy at this valence. (C) Transfer free energy reported from the sspB channel as a function of valence which is weighted by the number of sspB molecules (due to the number of mCherry molecules observed being proportional to each molecule's valence as opposed to the core where it is always constant at 24 GFPs). Red point represents extrapolated value and mean confidence error as determined in (B).

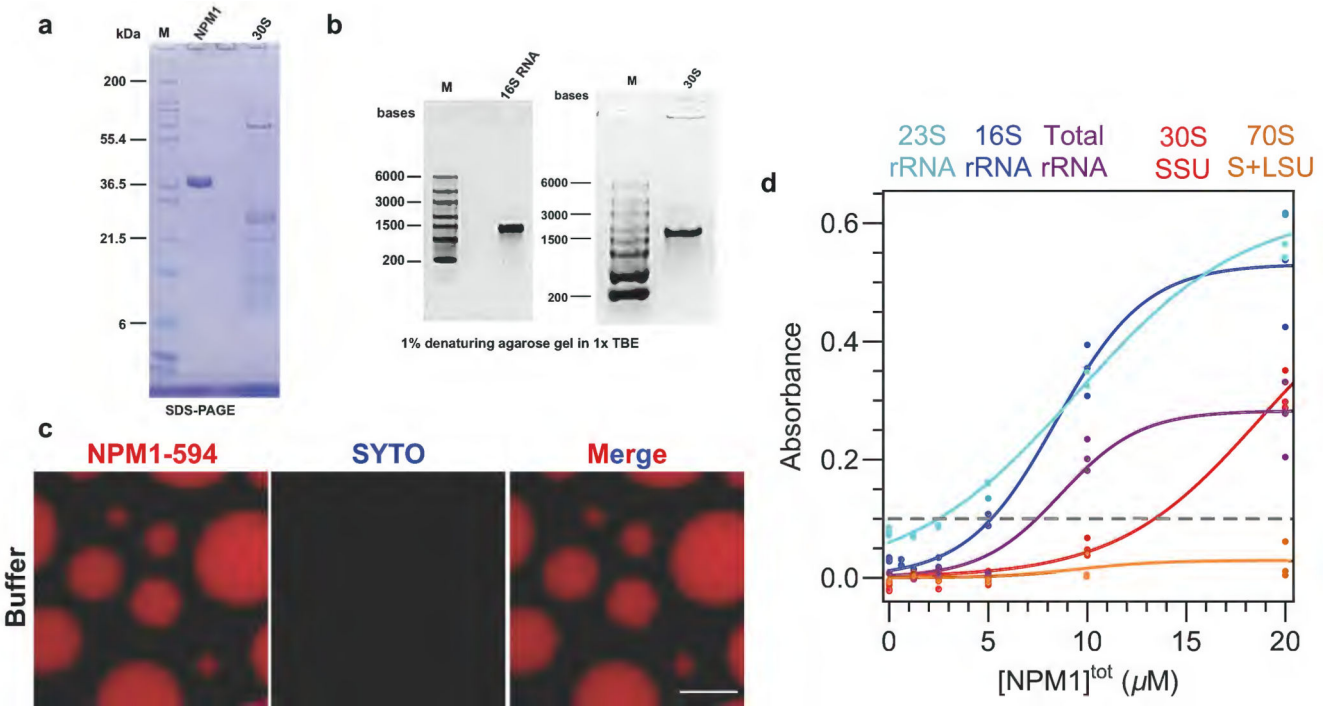

Figure 8. Controls for ribosomal mimics.

SDS-PAGE (A) and denaturing agarose gel (B) detailing purity of reagents used in experiments presented in Figure 4D and E. (C) Microscopy image for 10 μM NPM1–594 droplets formed with 5% PEG without any rRNA showing limited florescence indicating neither NPM1 nor PEG binds SYTO 40 and the droplet environment does not promote florescence of SYTO 40. (D) Phase separation assessed by turbidity at fixed 50 μg/ml indicated ribosomal substrate as a function of NPM1 concentration. The dashed gray line indicates where phase separation typically is observed in microscopy measurements.

Supplementary Material

Refer to Web version on PubMed Central for supplementary material.

Acknowledgements.

We thank members of the Brangwynne laboratory for helpful discussions and comments on this manuscript. This work was supported by the Howard Hughes Medical Institute, the St. Jude Collaborative on Membraneless Organelles, and grants from the NIH 4D Nucleome Program (U01 DA040601), and the Princeton Center for Complex Materials, an NSF supported MRSEC (DMR 1420541). L.Z. was supported by the NSF graduate fellowship (DGE-1656466). R.W.K acknowledges support from NIH [R01 GM115634, R35 GM131891 and P30 CA021765 (to St. Jude Children's Research Hospital)] and ALSAC. M.T. acknowledges support from NIH (F32 GM131524). Some images were acquired at the St. Jude Cell & Tissue Imaging Center, which is supported by SJCRH and NCI P30 CA021765; we would like to thank Drs. Victoria Frohlich and Jennifer Peters for their technical assistance. Data is available upon request.

Main References:

1. Shin Y. & Brangwynne CP Liquid phase condensation in cell physiology and disease. Science 357, (2017).

2. Banani SF, Lee HO, Hyman AA & Rosen MK Biomolecular condensates: organizers of cellular biochemistry. Nat. Rev. Mol. Cell Biol 18, 285–298 (2017). [PubMed: 28225081]
3. Nott TJ et al. Phase transition of a disordered nuage protein generates environmentally responsive membraneless organelles. Mol. Cell 57, 936–947 (2015). [PubMed: 25747659]
4. Shin Y. et al. Spatiotemporal Control of Intracellular Phase Transitions Using Light-Activated optoDroplets. Cell 168, 159–171.e14 (2017).
5. Wang J. et al. A Molecular Grammar Governing the Driving Forces for Phase Separation of Prion-like RNA Binding Proteins. Cell 174, 688–699.e16 (2018).
6. Bracha D. et al. Mapping Local and Global Liquid Phase Behavior in Living Cells Using Photo-Oligomerizable Seeds. Cell 175, 1467–1480.e13 (2018).
7. Holehouse AS & Pappu RV Functional Implications of Intracellular Phase Transitions. Biochemistry 57, 2415–2423 (2018). [PubMed: 29323488]
8. Alberti S, Gladfelter A. & Mittag T. Considerations and Challenges in Studying Liquid-Liquid Phase Separation and Biomolecular Condensates. Cell 176, 419–434 (2019). [PubMed: 30682370]
9. McSwiggen DT, Mir M, Darzacq X. & Tjian R. Evaluating phase separation in live cells: diagnosis, caveats, and functional consequences. Genes Dev. genesdev;gad.331520.119v1 (2019) doi:10.1101/gad.331520.119.
10. Oltsch F, Klosin A, Julicher F, Hyman AA & Zechner C. Phase separation provides a mechanism to reduce noise in cells. bioRxiv 524231 (2019) doi:10.1101/524231.
11. Feric M. et al. Coexisting Liquid Phases Underlie Nucleolar Subcompartments. Cell 165, 1686–1697 (2016). [PubMed: 27212236]
12. Mitrea DM et al. Nucleophosmin integrates within the nucleolus via multi-modal interactions with proteins displaying R-rich linear motifs and rRNA. Elife 5, (2016).
13. Flory PJ Principles of Polymer Chemistry. (Cornell University Press, 1953).
14. Wei M-T, Chang Y-C, Shimobayashi SF, Shin Y. & Brangwynne CP Nucleated transcriptional condensates amplify gene expression. http://biorxiv.org/lookup/doi/10.1101/737387 (2019) doi:10.1101/737387.
15. Kedersha N. et al. G3BP–Caprin1–USP10 complexes mediate stress granule condensation and associate with 40S subunits. J Cell Biol 212, 845–860 (2016). [PubMed: 27022092]
16. Choi J-M, Dar F. & Pappu RV LASSI: A lattice model for simulating phase transitions of multivalent proteins. PLoS Comput. Biol 15, e1007028 (2019).
17. Mao S, Kuldinow D, Haataja MP & Košmrlj A. Phase behavior and morphology of multicomponent liquid mixtures. Soft Matter 15, 1297–1311 (2019). [PubMed: 30506078]
18. Priftis D. & Tirrell M. Phase behaviour and complex coacervation of aqueous polypeptide solutions. Soft Matter 8, 9396–9405 (2012).
19. Jacobs WM & Frenkel D. Phase Transitions in Biological Systems with Many Components. Biophys. J 112, 683–691 (2017). [PubMed: 28256228]
20. Mitrea DM et al. Self-interaction of NPM1 modulates multiple mechanisms of liquid–liquid phase separation. Nat. Commun 9, 842 (2018). [PubMed: 29483575]
21. Lin Y-H, Brady JP, Forman-Kay JD & Chan HS Charge pattern matching as a ‘fuzzy’ mode of molecular recognition for the functional phase separations of intrinsically disordered proteins. New J. Phys 19, 115003 (2017).
22. Banerjee PR, Milin AN, Moosa MM, Onuchic PL & Deniz AA Reentrant Phase Transition Drives Dynamic Substructure Formation in Ribonucleoprotein Droplets. Angew. Chem. Int. Ed. Engl 56, 11354–11359 (2017). [PubMed: 28556382]
23. Ferrolino MC, Mitrea DM, Michael JR & Kriwacki RW Compositional adaptability in NPM1-SURF6 scaffolding networks enabled by dynamic switching of phase separation mechanisms. Nat. Commun 9, 5064 (2018). [PubMed: 30498217]
24. Banani SF et al. Compositional Control of Phase-Separated Cellular Bodies. Cell 166, 651–663 (2016). [PubMed: 27374333]
25. Geuskens M. & Bernhard W. Cytochimie ultrastructurale du nucléole: III. Action de l’actinomycine D sur le métabolisme du RNA nucléolaire. Exp. Cell Res 44, 579–598 (1966). [PubMed: 4960709]

26. Lazdins IB, Delannoy M. & Sollner-Webb B. Analysis of nucleolar transcription and processing domains and pre-rRNA movements by in situ hybridization. Chromosoma 105, 481–495 (1997). [PubMed: 9211976]

27. Burger K. et al. Chemotherapeutic drugs inhibit ribosome biogenesis at various levels. J. Biol. Chem 285, 12416–12425 (2010). [PubMed: 20159984]

28. Wei M-T et al. Phase behaviour of disordered proteins underlying low density and high permeability of liquid organelles. Nat. Chem. nchem.2803 (2017).

29. Zhu L. et al. Controlling the material properties and rRNA processing function of the nucleolus using light. Proc Natl Acad Sci USA 116, 17330–17335 (2019). [PubMed: 31399547]

30. Handwerger KE, Cordero JA & Gall JG Cajal bodies, nucleoli, and speckles in the Xenopus oocyte nucleus have a low-density, sponge-like structure. Mol. Biol. Cell 16, 202–211 (2005). [PubMed: 15509651]

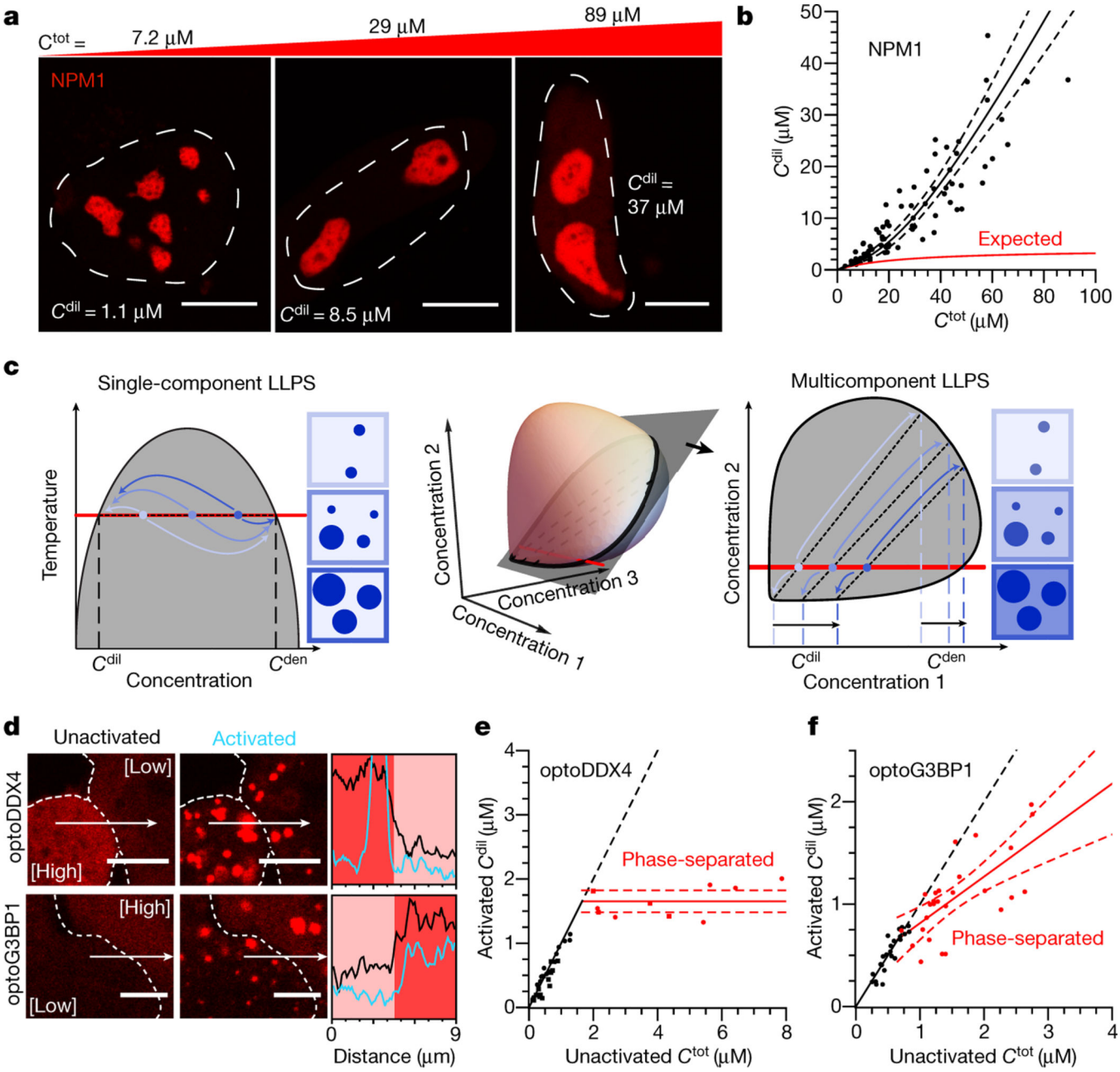

Figure 1. Multicomponent LLPS results in non-fixed C_{sat} and the emergence of a concentration-dependent phase stability.

(A) Example images of cells (from N=79 quantified in B) expressing NPM1-mCherry denoting total nuclear concentration (C^{tot}) and nucleoplasmic concentration (C^{dil}) of NPM1-mCherry in the top and within the image, respectively. The white dashed lines denote the nuclear boundary as defined by NPM1. Scale bar is 10 microns. (B) Concentration of NPM1-mCherry in the nucleoplasm (C^{dil}) with respect to the total NPM1-mCherry concentration in the nucleus (C^{tot}). The expected trend for a single C_{sat} is shown in red as described in the text. (C) Graphical representation of phase diagrams for both single and multicomponent LLPS showing fixed and non-fixed C^{dil} (or C_{sat}), respectively. Component

concentration changes along the red line; within the gray-shaded region, molecules phase separate into two phases whose concentrations (curved arrows) are defined by the dashed tie lines. For a multicomponent system, the 2-dimensional phase diagram is a slice of a higher dimensional one, resulting in skewed tie lines and non-fixed C_{sat}. (D) Example images of cells expressing OptoDroplet constructs with optoDDX4 (top row from N=19 quantified in E) or optoG3BP1 (bottom row from N=49 quantified in F) with the cytoplasmic (circles)/ nucleoplasmic (squares) concentrations before and after full activation, respectively. Cells shown as red points exhibit condensates upon activation (none had condensates prior to activation); dashed lines represent mean confidence intervals for cells with foci for constant and linear fits in optoDDX4 and optoG3BP1, respectively. OptoG3BP1 experiments are arsenite-stressed cells with G3BP1A/B knocked out; optoDDX4 data reproduced from[14]. Here scale bars are 5 microns. Line scans shown correspond to intensity traces before and after activation in black and blue, respectively.

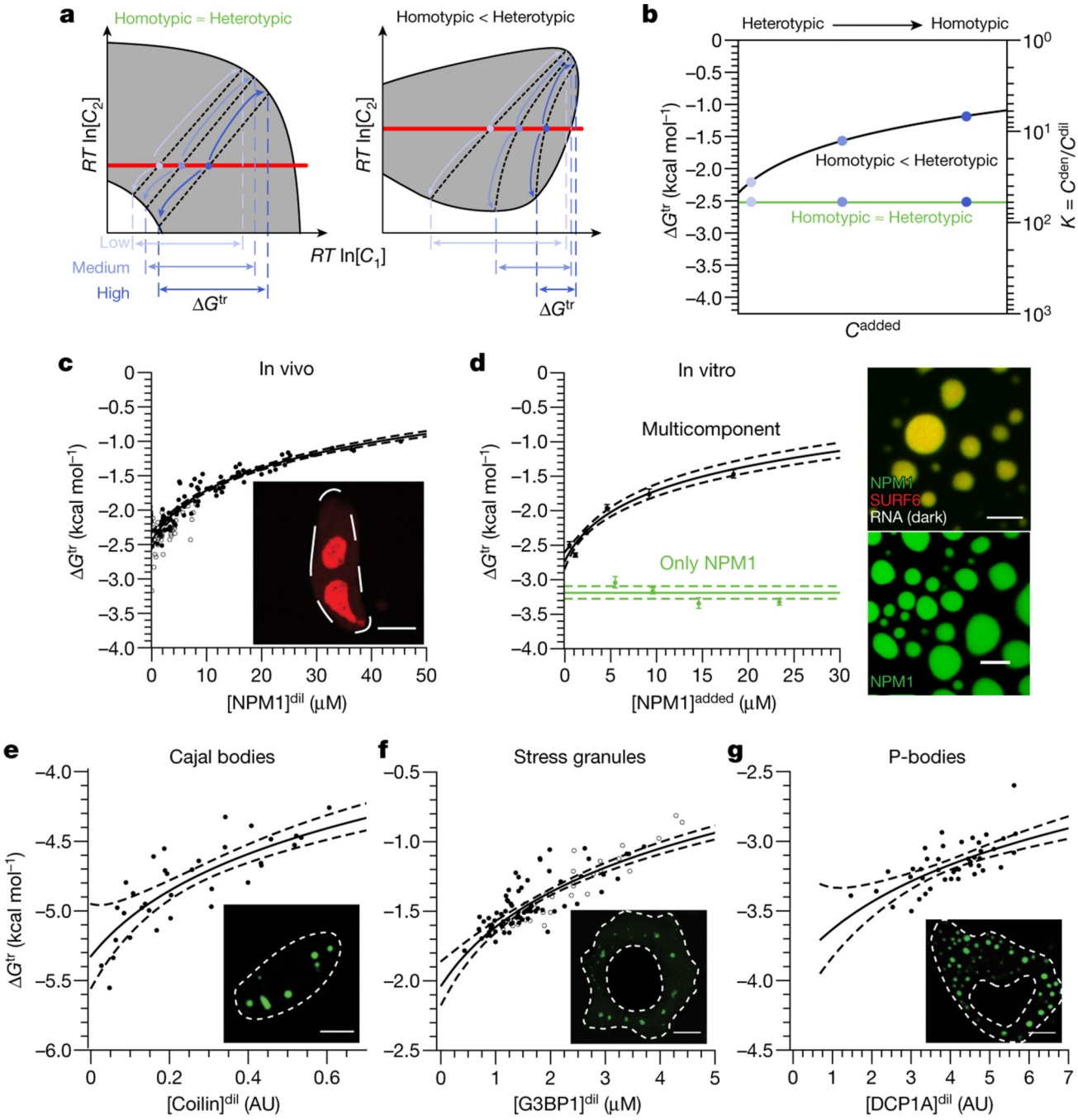

Figure 2. Determining the contribution of heterotypic and homotypic interactions driving condensate formation *in vivo* and *in vitro*.

(A) Schematic illustrating the connection between the phase diagram and the transfer free energy of a component when heterotypic interactions are equal (left) to or stronger (right) compared to homotypic interactions. (B) Accompanying schematic detailing the qualitative change in the transfer free energy of component 1 (*i.e.* C_1 in A) with an increase in its expression for the two cases in (A). (C) Thermodynamic dependence of NPM1 (-mCherry filled, -GFP empty) transfer from the nucleoplasm into the nucleolus, as a function of its increased expression (concentration in the nucleoplasm). Inset, image from Fig 1A to

highlight that these data represent a reanalysis of those experiments. (D) *In vitro* reconstitution experiments showing ΔG^{tr} for NPM1 as a function of added NPM1. Image of NPM1 droplets with 5% PEG (bottom right) and of ternary NPM1:SURF6N:rRNA droplets in buffer (top right). ΔG^{tr} for Coilin-EYFP (E), G3BP1 (F, -GFP empty, -mCherry filled), and DCP1A-EYFP (G) from the dilute phase (*i.e.* nucleoplasm or cytoplasm) to Cajal bodies, arsenite-induced Stress granules, and P-bodies (*i.e.* dense phases), respectively. For all proteins here, a higher C^{dil} results from an increase in its expression (Fig 1B, Extended Data Fig. 2A-C). All scale bars are 10 microns.

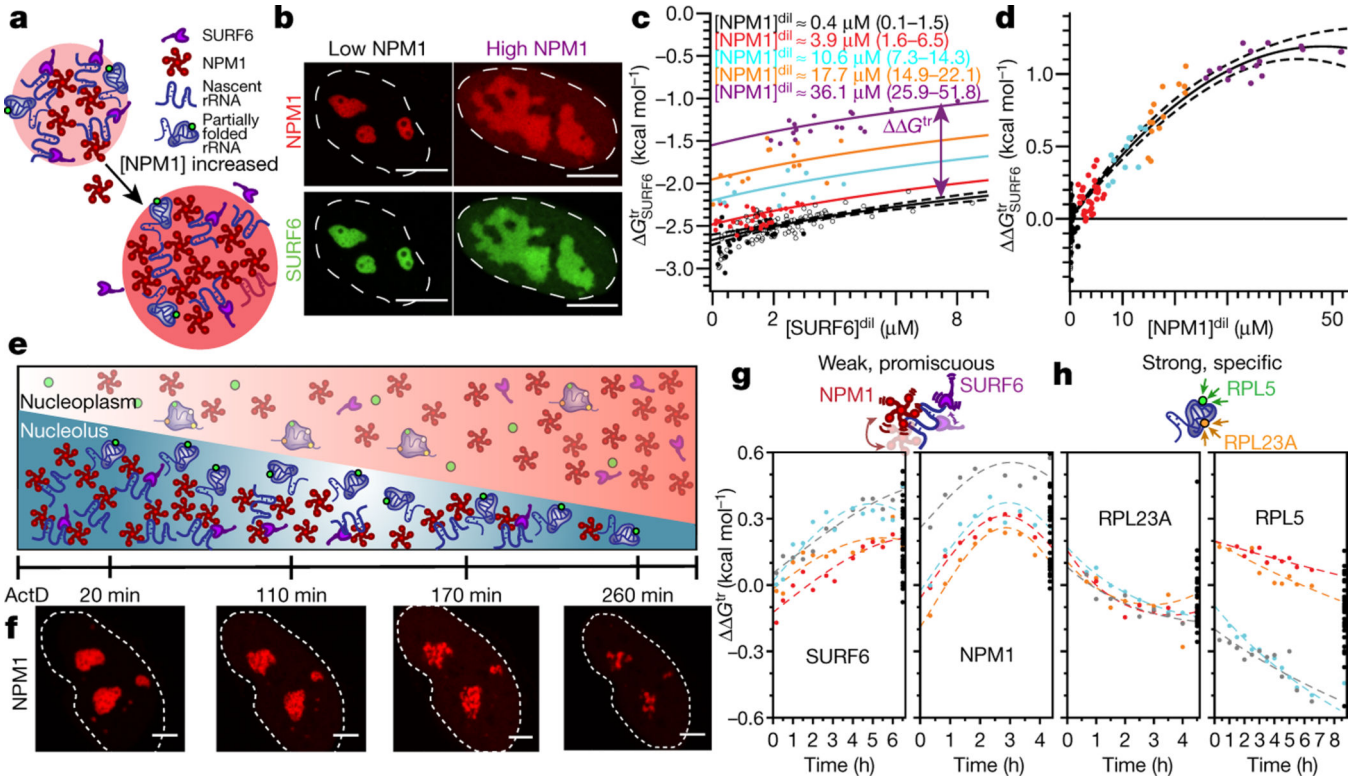

Figure 3. Heterotypic interactions between nucleolar proteins and rRNA underly nucleolar thermodynamics.

(A) Schematic of proposed mechanism for the dilution of non-NPM1 molecular interactions in the dense phase due to NPM1 overexpression. Only relevant species shown for clarity. (B) Example images for cells (from N=102 quantified in C/D) expressing NPM1-mCherry and SURF6-GFP with high and low expression of NPM1 as indicated. Scale bar is 10 microns. (C) Change in the transfer free energy of SURF6 with overexpression of NPM1 plotted against SURF6 concentration (colors are different concentrations of NPM1 in μM as indicated with mean and range values, open circles are cells without additional NPM1 expressed). The method of calculating $\Delta\Delta G^{tr}$ at a referenced nucleoplasmic SURF6 concentration is shown via arrows and displaced lines in (C) and (D) shown as a function of NPM1 concentration with the same colored concentrations as C. (E) Schematic of ActD treatment on nucleoli with time. (F) Images of cells at indicated times post ActD treatment (from N=4 NPM1-tagged time series). Corresponding quantification for NPM1 cells is shown in Extended Data Fig. 5. Scale bar is 5 microns. Dependence of $\Delta\Delta G^{tr}$ of (G) NPM1 and SURF6 and (H) RPL23A and RPL5 with ActD treatment. Each color for each plot represents an individual cell followed with time. Black points are cells measured at the indicated time points. Schematics highlighting the differences in suggested interactions with rRNA are shown above G and H.

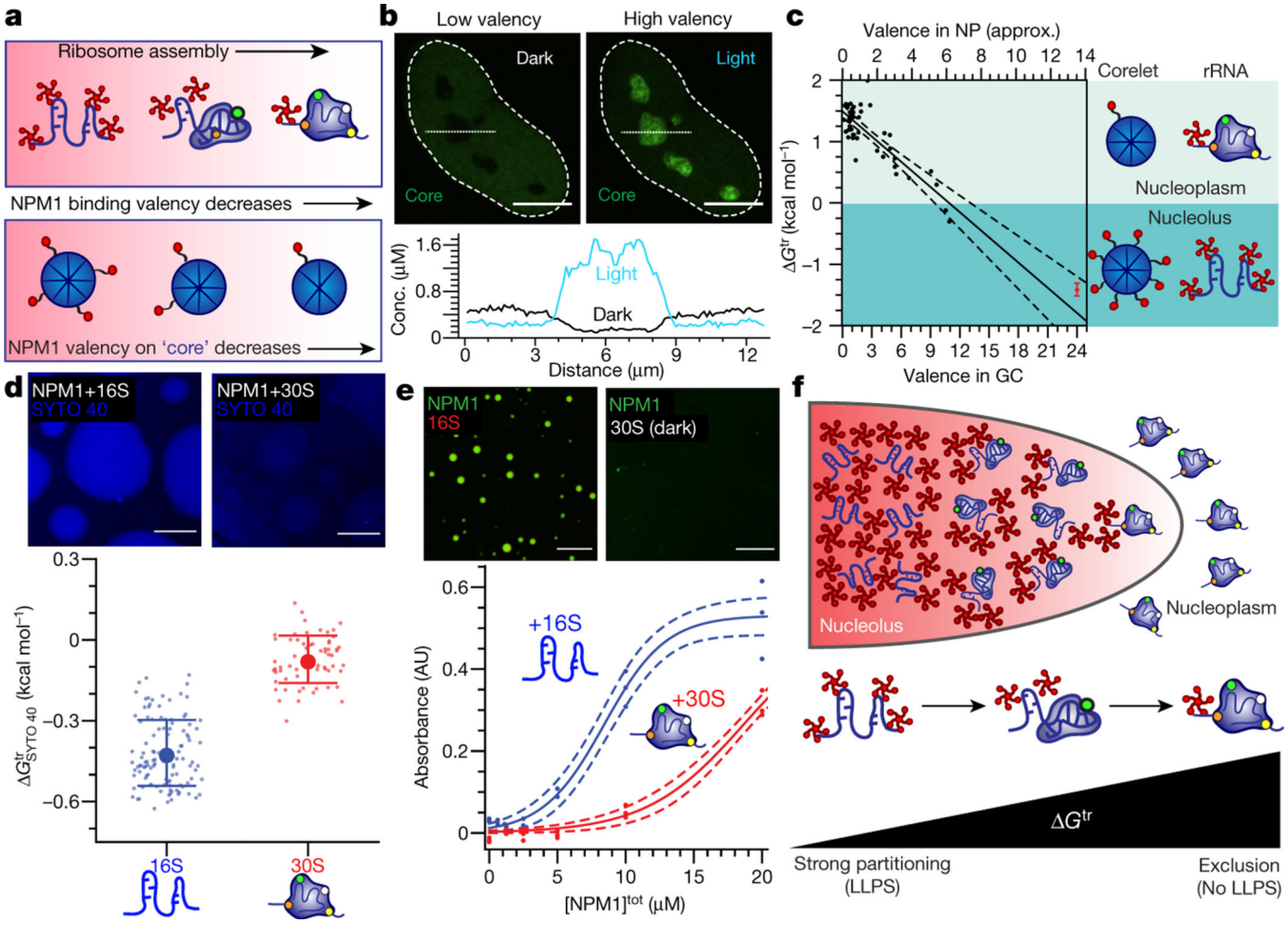

Figure 4. Composition-dependent heterotypic LLPS drives specific ribosomal subunit exclusion.

(A) Top, schematic NPM1 valency as a function of rRNA folding/processing in the nucleolus and bottom, schematic of NPM1 valency on ferritin "cores" using the Corelet optogenetic system. (B) Images of a cell highlighting the partitioning of the "cores" (ferritin-iLID-GFP) before light (*e.g.* low effective valence) and after light (*e.g.* high effective valence) upon which NPM1-C binding sites on the core are saturated in this cell. Quantification is shown below corresponding to the dashed line shown in the images. (C) Corresponding quantification of the dependence for the ΔG^{tr} of the core as a function of the valence in the GC after light activation. Dotted lines are fits to data. (D) ΔG^{tr} measured by incubation with 6.5 μM SYTO 40 to approximate the transfer free energies of 16S rRNA or the 30S small ribosomal subunit (at a total of 5 μg/ml) into droplets formed with NPM1 (10 μM) and 5% PEG droplets as indicated. Error bars represent standard deviation from N=118, 64 droplets for 16S and 30S, respectively. Top representative images. (E) Turbidity assay of indicated concentration of NPM1 with either the 16S rRNA or the 30S small ribosomal subunit in blue and green, respectively. 50 μg/ml of the RNA species is added; validation of protein and RNA components in Extended Data Fig. 7. 16S is labeled via a morpholino approach as described in the methods. Top, microscopy images with 10 μM NPM1 with

indicated RNA species. (F) Proposed mechanism for ribosomal subunit exclusion from the GC of the nucleolus driven by thermodynamics of nucleolar LLPS.